Materials Today Bio 30 (2025) 101393

Contents lists available at ScienceDirect

Materials Today Bio

journal homepage: www.journals.elsevier.com/materials-today-bio

Magnetic field-induced synergistic therapy of cancer using magnetoplasmonic nanoplatform

Siqi Gao [a,1], Iuliia Golovynska [a,1], Jiantao Liu [a], Zhenlong Huang [a], Hao Xu [a], Jinghan Qu [a], Fangrui Lin [a], Galyna Ostrovska [b], Junle Qu [a], Tymish Y. Ohulchanskyy [a,*]

[a] Key Laboratory of Optoelectronic Devices and Systems of Ministry of Education and Guangdong Province, College of Physics and Optoelectronic Engineering, Shenzhen University, Shenzhen, 518060, China

[b] Institute of Biology and Medicine, Taras Shevchenko National University of Kyiv, Kyiv, 01601, Ukraine

ARTICLE INFO

Keywords:
Magnetoplasmonic nanoparticles
Magnetophoretic movement
Targeted drug delivery
Magnetic field-induced aggregation
Near infrared photothermal therapy
Synergistic cancer therapy

ABSTRACT

Combining photothermal and chemotherapy using single nanoplatform is an emerging direction in cancer nanomedicine. Herein, a magnetic field (MF) induced combination of chemo/photothermal therapy is demonstrated using Fe_3O_4@$mSiO_2$@Au core@shell@satellites nanoparticles (NPs) loaded with chemotherapeutic drug doxorubicin (DOX), both *in vitro* and *in vivo*. An application of an external MF to the NPs dispersion causes magnetophoretic movement and aggregation of the NPs. While the synthesized NPs only slightly absorb light at ~800 nm, their aggregation results in a significant near infrared (NIR) absorption associated with plasmon resonance coupling between the Au satellites in the NPs aggregates. As a result, the aggregates revealed an enhanced photothermal conversion efficiency (~67 % versus ~19 % for NPs in absence of MF) and an enhanced NIR photothermal effect was observed under 808 nm laser irradiation. A combination of the MF induced NIR photothermal therapy (PTT) with DOX chemotherapeutic action resulted in an efficient killing of NPs treated cancer cells *in vitro* and tumor growth restriction in 4T1-tumor-bearing mice *in vivo*. Histological studies showed striking differences in development and malignancy between tumors treated with the combination of NPs, MF and an 808 nm laser, and the control treatments, revealing a synergy of the MF-induced NIR PTT and chemotherapy and suggesting a promising strategy for cancer therapy.

1. Introduction

Cancer is regarded as a major threat to human health worldwide due to the increasing incidence and mortality rate [1]. While novel anticancer strategies (e.g., immunotherapy and gene therapy) are emerging, chemotherapy is still considered a common and effective treatment method [2–4]. At the same time, the shortcomings of traditional chemotherapy, such as systemic toxicity and lack of tumor selectivity, hinder its applications in clinical treatment. Moreover, a single chemotherapy regimen may not be enough to completely suppress tumors [5]. On the other hand, the rise of nanotechnology allows for other cancer therapeutic avenues, such as photodynamic therapy (PDT) and photothermal therapy (PTT), which have been introduced, along with diagnostic modalities, in cancer nanotheranostic applications [6–9]. PTT is a treatment strategy to efficiently kill tumor cells via converting light into heat. The therapeutic effect of the PTT nanoplatform can be controlled by tuning photothermal conversion efficiency [10,11], with a precise increase in temperature allowing for localized and efficient killing of tumor cells. Importantly, combination of PTT with chemotherapy on the same nanoplatform can results in a significantly enhanced cancer treatment efficacy, along with lower systemic toxicity in comparison with chemotherapy alone. In addition, an introduction of cancer drug nanocarriers can not only lead to a prolonged systemic circulation and higher tumor accumulation through the enhanced permeability and retention (EPR) effect, but also enhance the cellular uptake and allow for a stimuli-responded drug release [12–16].

It should be noted that an application of external magnetic field (MF) is considered a simple but efficient method to target cancer cells *in vitro* and *in vivo*. MF, as an external stimulus for magnetic targeted tumor chemotherapy, can enhance the targeting efficiency and accelerate the accumulation of drugs at tumor site [17–19]. The magnetic targeting methods have also been investigated for chemotherapy/PDT/PTT of

* Corresponding author.
E-mail address: tyo@szu.edu.cn (T.Y. Ohulchanskyy).
[1] Contributed equally to this work.

https://doi.org/10.1016/j.mtbio.2024.101393
Received 17 August 2024; Received in revised form 25 November 2024; Accepted 7 December 2024
Available online 7 December 2024

cancer cells *in vitro* and *in vivo* [17,20–22]. The incorporation of magnetic moieties into a therapeutic nanocarrier can allow for using MF as an external stimulus to synergistically enhance efficiency of PDT, PTT or chemotherapy/PDT/PTT combination delivered with the nanoformulation [23–25]. Recently, Y. Li and colleagues proposed a multifunctional nanoplatform of Fe_3O_4@NDs-DOX core@shell nanoparticles (NDs: nanodiamonds, DOX: anticancer chemotherapy drug), which allowed for MF-induced chemotherapy/PTT combination with the assistance of an MF, exploiting that Fe_3O_4@NDs-DOX nanoparticles (NPs) gathered in MF-applied tumor more efficiently [23].

On the other hand, a single nanoplatform combining magnetic and plasmonic features can not only provide a magnetophoretic response under applied MF, but can also deliver PTT through plasmonic absorption that can be controllably tuned during synthesis [26–28]. Muzzi and co-workers reported a star shape magnetic-plasmonic Au@Fe_3O_4 nano-heterostructures for PTT, taking advantage of coating of the Fe_3O_4 shell can achieve the shift of the plasmonic resonance of the Au core to 640 nm, which is the largest red shift achievable in Au@Fe_3O_4 homogeneous core@shell nanoformulations, prompting application in PTT in the first biologically transparent window [25]. Ohulchanskyy with colleagues reported a magnetoplasmonic nanoplatform combining gold nanorods (GNR) and iron-oxide NPs within phospholipid-based polymeric nanomicelles (PGRFe). An external magnetic field application was shown to cause an enhanced uptake of the magnetoplasmonic formulation by cancer cells *in vitro*. In addition, under NIR laser irradiation, the magnetoforetically attracted PGRFe formulation efficiently generates heating associated nano/micro bubbles within cancer cells, killing them [29]. Hence, the combination of magneto and plasmonic constituents can be used synergistically: the simultaneous application MF and NIR laser irradiation can produce the heating, potentially increasing the efficiency of the magnetoplasmonic nanoformulations PTT [6,30–32].

Despite considerable progress in the development of magnetically driven nanoplatforms delivering chemotherapy/PTT combination [33,34], there are still problems to overcome. In particular, a relatively lower absorptivity of the photothermal agents (PTAs) at the desired wavelengths of irradiation (e.g., in NIR region) results in a high and unsafe irradiation laser fluence and/or high concentrations, which are required to achieve a desirable PTT effect. As a result, excessively high temperatures can be locally generated, which can damage healthy tissues. In addition, high concentration of PTAs suggests a low biocompatibility and short and/or long term *in vivo* systemic toxicity. Recently, Ohulchanskyy and Mukha with colleagues reported a magnetoplasmonic nanocomposites (MPNC), which contain nanosized Fe_3O_4 and gold constituents, showed an ability to be magnetophoretically controlled and concentrated using the external magnetic field. A magnetically-induced formation of the MPNC aggregates leads to an increase in optical absorption in NIR spectral range (800–1000 nm), which disappears when magnetic field is removed. This increase in NIR absorption caused by the magnetically induced in situ aggregation of MPNC, suggests an approach of the magnetic field enhanced NIR-activated photothermal therapy of cancer and other diseases, as it was illustrated by the magnetic field enhanced photothermal effect in MPNC colloids. Furthermore, the magnetic field-induced concentration of MPNC on the surface of cultured cancer cells, followed by irradiation of the cells with scanning laser, led to a pronounced photothermal effect, which caused microbubble formation and membrane damage in the cancer cells [35]. However, the bonding between magnetic and plasmonic constituents within MPNC was not very strong, suggesting that MPNC can disassemble *in vivo*. In addition, F. Lu with colleagues reported a multi-functional hollow mesoporous silica nanocapsules with encapsulated iron oxide (Fe_3O_4@mSiO_2) for providing an excellent nanoplatform for the combination of hyperthermia and chemotherapy, which allowed for MF-triggered the accelerated release of drug and induced the local heating [36].

Herein, we introduced a magnetic field-induced combinational (chemotherapy/NIR PTT) killing of cancer cells *in vitro* and *in vivo* using magnetoplasmonic nanoformulation (MPNF) prepared by a layer-by-layer method and containing a Fe_3O_4 nanoparticle as an inner core, a layer of mSiO_2 as the intermediate shell, and Au seeds decorating mSiO_2 as an outer satellites shell. After MPNF preparation, the anticancer drug DOX was loaded in the mesoporous silica shell (Scheme 1). The synthesized Fe_3O_4@mSiO_2@Au-DOX core@shell@satellites NPs displayed a negligible NIR absorption and no photothermal (PT) effect was caused by NIR irradiation (808 nm laser diode) in absence of an external MF. In contrast, the application of an external MF led to a noticeable increase in NIR absorption due to the MF-induced aggregates of Fe_3O_4@mSiO_2@Au-DOX NPs and correspondent plasmon resonance coupling in the adjacent Au NPs [37–39]. Along with the enhanced NIR absorption, an increased photothermal conversion efficiency of the MF-induced NPs aggregates was found, resulting in a greatly increased NIR PT effect, which has been applied by us for MF-induced NIR PTT. In the *in vitro* and *in vivo* studies, the MF induced and tumor targeted NIR PTT was combined with the chemotherapeutic action of DOX and the most powerful anticancer effect was achieved using Fe_3O_4@mSiO_2@Au-DOX NPs under 808 nm laser irradiation following MF application. The *in vitro* and *in vivo* results, along with histological studies, revealed a synergy of the combination of MF-induced NIR PTT and chemotherapy delivered with MPNF. It should be emphasized that our study differs from the previous reports on magnetically driven nanoplatforms delivering chemotherapy/PTT combination as revealed and exploited strong enhancement of NIR absorption of the magnetopasmonic NPs when the external magnetic field was applied. This enhancement was caused by an aggregation of the NPs, which resulted in plasmon resonance coupling between the Au NPs within the aggregates. Thus, the MF-induced and localized appearance of NIR plasmonic absorption provides a possibility for a strong NIR photothermal effect, efficient and MF-targeted (localized) NIR PTT, and, correspondingly, a synergistically enhanced targeted cancer therapy.

2. Materials and methods

2.1. Materials

1-octadecene (ODE), dibenzyl ether, 1-tetradecene, iron (III) acetylacetonate ($Fe(acac)_3$), oleic acid (OA), anhydrous ethanol, hexane, chloroform, methylene chloride, dimethylformamide (DMF), cetyltrimethylammonium bromide (CTAB), triethanolamine (TEA), tetraethyl orthosilicate (TEOS), (3-mercaptopropyl) trimethoxysilane (MPTES), ammonium nitrate, chloroauric acid ($HAuCl_4$), sodium citrate, sodium borohydride ($NaBH_4$), and anti-cancer chemotherapy agent doxorubicin (DOX) were purchased from Sinopharm Chemical Reagent Co (China). All reagents were directly used without purification. A rectangular (20 × 10 × 4 mm) and a round (5 mm diameter, 1 mm thick) NdFeB magnets were purchased from Taobao and used for *in vitro* and *in vivo* experiments, respectively.

2.2. Synthesis of Fe_3O_4

Fe_3O_4 nanoparticles were synthesized according to previously reported method [40–42]. In brief, a mixture of ODE (50 mL), dibenzyl ether (50 mL), and 1-tetradecene (15 mL) was used as a high-boiling solvent. Then, $Fe(acac)_3$ (5 mmol), and OA (20 mmol) were added in the mixed solvent. This resulting mixture was heated to 70 °C under a vacuum and kept at this temperature for 1h with vigorous magnetic stirring. Subsequently, the temperature of the mixture was increased to 290 °C under a constant flow of argon gas and kept at this temperature for another 1 h. Finally, the mixture was cooled to room temperature under a constant flow of argon gas. The purification of the iron oxide was performed by adding anhydrous ethanol, the black mixture was centrifugation at 12000 rpm for 20 min, and then the product was washed several times with a mixture of anhydrous ethanol and hexane to remove the residual reactants. Finally, iron oxide was dissolved in

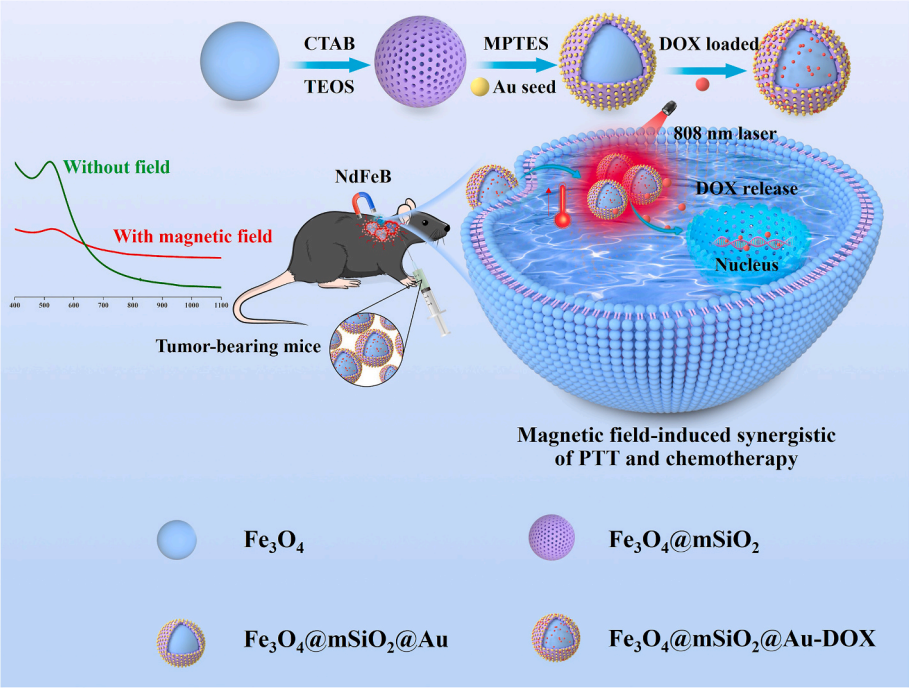

Scheme 1. Synthesis of Fe_3O_4@mSiO_2@Au-DOX nanoformulation and its use for the enhanced synergistic cancer therapy induced by locally applied magnetic field causing aggregation of magnetoplasmonic NPs in situ.

chloroform and stored in a refrigerator at 4 °C.

2.3. Preparation of Fe_3O_4@mSiO_2

Fe_3O_4@mSiO_2 nanoparticles were synthesized according to previously reported method [43]. Firstly, CTAB (0.4 g) and TEA (0.06 g) were dissolved in deionized water (20 mL) under magnetic stirring, and then iron oxide (2 mg, in 1 mL chloroform) was added to the above solution, the mixed solution was continuously sonicated for 30 min. The chloroform in the system was removed by a rotary evaporator (80 °C). After these injections, the resulting solution was kept at 80 °C for 1 h under magnetic stirring, and the TEOS (100 μL) was added dropwise into the above solution. The reaction system was stirred for 4 h in the thermostatic water bath at 80 °C. The product was collected by centrifugation (12000 rpm, 10 min) and washed several times with ethanol. To remove the surfactants (CTAB), the Fe_3O_4@mSiO_2 solution was obtained by stirring in a solution of ammonium nitrate in ethanol (1 wt%, 3 h) for two rounds.

2.4. Preparation of MPTES-modified Fe_3O_4@mSiO_2

Fe_3O_4@mSiO_2-SH nanoparticles were synthesized according to previously reported method [44–46]. Fe_3O_4@mSiO_2 nanoparticles (1 mg) were dispersed in ethanol by ultrasonication for 30 min. Next, MPTES (100 μL, 10 % in ethanol) was added to the Fe_3O_4@mSiO_2 solution and sonication continued for another 20 min. The resulting solution was placed in the shaker at room temperature for two days. Then, the obtained Fe_3O_4@mSiO_2-SH nanoparticles were washed three times with ethanol to remove the unbound organosilane reagents and redispersed into 10 mL ethanol.

2.5. Preparation of Fe_3O_4@mSiO_2@Au

A small size of Au NPs was prepared by following the steps [47], 20 mL solution of $HAuCl_4$ (0.25 mM) and sodium citrate (0.25 mM) were mixed under vigorous magnetic stirring. Then, 0.6 mL of freshly prepared 100 mM $NaBH_4$ solution was added to the above solution. The formation of Au NPs was confirmed by observing the change in its color from pink to light red. Finally, the resulting mixture was continuously stirred for 30 min at room temperature. 1 mL of the prepared Fe_3O_4@mSiO_2-SH solution was added dropwise into 3 mL of fresh Au nanoparticle solution, and the mixed solution was continuously sonicated for 30 min. Then, the reaction was carried out with vortex stirring for 12 h. Finally, the obtained product was washed with water three times and redispersed in the deionized water.

2.6. Characterization

The absorption spectra were measured with a UV–Vis spectrophotometer LAMBDA 750 (PerkinElmer, USA). Emission spectra were recorded using a Fluorolog-3 spectrofluorometer (Horiba, Japan). DLS and Zeta potential were performed using a Nano-ZS90 Zetasizer (Malvern Panalytical, United Kingdom). Transmission electron microscopy (TEM) was performed using a JEM2100PLUS TEM instrument (JEOL, Japan). Elemental mapping analyses was performed using a JEM-F200 (HRP) instrument. Magnetization measurements were performed using a vibrating sample magnetometer (VSM-Lakeshore 7404). Fluorescence and brightfield microscope images were obtained using a Nikon Eclipse Ti-U inverted fluorescence microscope equipped with a Nikon Digital Sight DS-Fi2 camera (Nikon, Tokyo, Japan) and analyzed with NIS-Elements D 4.50.0064-bit software. PT images were acquired with a FLIR A310 thermal camera (FLIR, Wilsonville, OR, USA).

2.7. Drug loading

For more efficient DOX loading to NPs, it was first converted to the hydrophobic form as previously described [48]. For this purpose, 377 μL of TEA was added into an aqueous solution of DOX hydrochloride (50 μg of DOX HCl in 3 mL of H_2O). After keeping the reaction mixture at room temperature overnight, 10 mL of methylene chloride were added to the solution. Then, the organic phase was separated and DOX powder was formed after CH_2Cl_2 evaporation. 5 mL of as-synthesized Fe_3O_4@mSiO_2@Au nanocomposites were mixed with hydrophobic DOX (150 μL, 2 mM in DMF) and stirred at room temperature for 24 h. The

DOX-loaded Fe_3O_4@mSiO_2@Au nanocomposites were collected by centrifugation at 12000 rpm for 15 min and washed two times with water to remove the unbound DOX and then a supernatant solution was collected. The mass of loaded DOX into the Fe_3O_4@mSiO_2@Au nanocomposites was determined by a UV–Vis spectrophotometer at DOX absorbance peak at 490 nm. DOX loading efficiency for Fe_3O_4@mSiO_2@Au was determined using the following equation.

$$\text{DOX loading efficiency } (\%) = \frac{\text{mass of loaded DOX}}{\text{mass of feed DOX}} \times 100\%$$

2.8. In vitro studies

Human cervical cancer cells (HeLa) were purchased from Procell Life Science and Technology (China) and were used for the *in vitro* cell experiments. HeLa cells were cultured in DMEM, supplemented with 10 % FBS, 1 % glutamax, and 1 % antibiotic-antimycotic at 37 °C in a 95 % humidified atmosphere with 5 % CO_2. First, the biocompatibility of Fe_3O_4@mSiO_2@Au-DOX was evaluated by CCK-8 assay. HeLa cells were seeded into 96-well plates at a density of 1×10^3 cells/well and incubated for 24 h with 5 % CO_2 at 37 °C. Then, all cell medium was replaced with fresh medium containing Fe_3O_4@mSiO_2@Au-DOX (50 μg/mL, DOX = 2 μM). To introduce magnetic field, a NdFeB magnet was placed the 96-well plate bottom. After incubation for another 12 h, the CCK-8 reagent (10 μL) was added to each well and incubated for 1 h at 37 °C for the observation of cell viability change. Assessment of cell viability were performed using Automated Cell Counter TC20TM.

To assess cellular uptake of Fe_3O_4@mSiO_2@Au-DOX NPs, HeLa cells were seeded into 35 mm petri dishes in the DMEM cell medium. After culturing for 12 h, the cell medium was replaced with a fresh medium containing Fe_3O_4@mSiO_2@Au-DOX NPs and the NPs treated cells were incubated for 12 h at 37 °C with 5 % CO_2. After incubation, the cells were rinsed, fresh medium added and imaged on Nikon Eclipse Ti-U inverted microscope. The DOX fluorescence was imaged using a band-pass filter (577 nm–633 nm).

2.9. In vivo studies

All animal studies were performed with the requirement of the Animal Ethical and Welfare Committee of Shenzhen University (Approval No. SZUHSC-01). Female nude mice (4–6 weeks old) were used for *in vivo* studies. 4T1 tumor cells (2×10^6) were selected for the injection into the back of mice. The following therapy studies were performed after the size of tumor growth was about 100 mm^3 for ten days.

For assessment of therapy effect *in vivo*, the 4T1 tumor-bearing mice were randomly divided into five groups for different treatment: (1) intratumoral injection of PBS, with 808 nm laser irradiation; (2) intratumoral injection of Fe_3O_4@mSiO_2@Au, with 808 nm laser irradiation; (3) intratumoral injection of Fe_3O_4@mSiO_2@Au-DOX, with 808 nm laser irradiation; (4) intratumoral injection of Fe_3O_4@mSiO_2@Au, with MF application and 808 nm laser irradiation; (5) intratumoral injection of Fe_3O_4@mSiO_2@Au-DOX, with MF application and 808 nm laser irradiation. Three hours after the injection at groups 1, 2, 3, 4, and 5 were irradiated with 808 nm laser (0.3 W/cm^2) for 20 min and the corresponding thermal images were obtained. Next day, the same laser irradiation experiment was conducted on groups 1, 2, 3, 4, and 5. The therapeutic effects were assessed by monitoring the mice's body weight and tumor volume changes every day. The tumor volume change was calculated by the equation: tumor volume $= \frac{1}{2}$ length $\times$ width^2. In the therapy process, the mice were sacrificed when the tumor size of mice grew to the maximum permitted size of 15 mm [49,50]. Immediately after mice were sacrificed, the tumors were extracted. For histological tumor examination, a standard formalin-fixed paraffin-embedding method was used. Briefly, samples were fixed in 4 % PFA, then rinsed in PBS, dehydrated in increasing concentrations of ethanol (70 %, 80 %, 90 %, 96 %), cleared in xylene, soaked in paraffin wax and embedded in boxes with paraffin (Thermo Fisher Scientific, USA). Serial slices (4 μm thickness, 10 slices per tumor) were obtained with a microtome and serially glued onto slides. The slices were stained with hematoxylin and eosin (H&E) according to the standard method. Representative histological images were obtained using an inverted Nikon fluorescence microscope and analyzed with ImageJ software. In addition, the blood samples were collected for routine blood analysis.

2.10. Statistical analysis

All data were presented as the mean standard deviation (SD) from at least three independent experiments ($n \geq 3$). The statistical differences in the data were determined using a One-Sample *t*-Test analysis within Origin 9_64 software. *$p < 0.05$, **$p < 0.01$, and ***$p < 0.001$ were considered statistically significant.

3. Results and discussion

3.1. Synthesis of Fe_3O_4@mSiO_2@Au

Fe_3O_4@mSiO_2@Au core@shell@satellites NPs were prepared by a layer-by-layer method using iron oxide, mesoporous silica, and gold as substrates. First, monodispersed hydrophobic Fe_3O_4 NPs were synthesized by the thermal decomposition method that allows for obtaining dispersion of nanoparticles with uniform size distribution [51]. As it was revealed by transmission electron microscopy (TEM), the obtained Fe_3O_4 NPs did have a uniform size (the average diameter of 8 nm, Fig. 1a and Fig. S1 in Supporting Information). Next, a surfactant CTAB was used for the ligand exchange with the oleic acid group of Fe_3O_4. Through a following process of hydrolysis and condensation of tetraethyl orthosilicate (TEOS) in water/triethanolamine (TEA) and with the use of a reverse microemulsion method [52–55] a uniform silica shell (~18 nm thick) covered on the surface of Fe_3O_4, which resulted in the formation of Fe_3O_4@mSiO_2 core@shell nanoparticles (Fig. 1b and Fig. S2). The silica shell thickness could be easily controlled by adjusting the concentration ratio of Fe_3O_4/TEOS. Finally, MPTES was used as a silane coupling reagent, which provided negatively charged sulfhydryl groups on the silica surface, allowing for attachment of the pre-synthesized gold NPs (Fig. S4) through formation of a strong Au-S bond. In such a way, Fe_3O_4@mSiO_2@Au NPs with core@shell@satellites structure were successfully synthesized (Fig. 1c). The formation of Fe_3O_4@mSiO_2@Au NPs has also been confirmed by EDX spectroscopy and mapping (Fig. S3, Fig. 1d), which indicates that the Fe element is located in the core, whereas the Si is shown to be around Fe, due to the formation of the silica shell. The gold seeds are uniformly adsorbed on the surface of Fe_3O_4@mSiO_2 core@shell NPs. Furthermore, X-ray photoelectron spectroscopy (XPS) was employed to assess the chemical composition of Fe_3O_4@mSiO_2@Au NPs (Fig. S5(a)). The corresponding Fe 2p, O 1s, Si 2s, Si 2p and Au 4f peaks can be observed in the full spectrum XPS of the Fe_3O_4@mSiO_2@Au NPs, indicating the presence of Fe, O, and Au elements. As shown in Fig. S5(b), after the Fe_3O_4 core is coated with a mSiO_2 shell, the Fe 2p peak becomes almost unidentifiable due to the shallow XPS detection depth limit of 10 nm [56]. However, a clear Si 2p peak (102.1 eV) is observed due to the Si element from the mSiO_2 shell (Fig. S5(c)). Then, the high-resolution Au 4f spectra reveals that Au 4f 7/2 (82.8 eV) and 4f 5/2 (86.5 eV) binding energies are observed from Fig. S5(d), indicating the presence of Au satellites in Fe_3O_4@mSiO_2@Au NPs. Based on the TEM, EDX, and XPS results, we concluded that the Fe_3O_4@mSiO_2@Au NPs with the core@shell@satellites structure were successfully synthesized.

The size of Fe_3O_4, Fe_3O_4@mSiO_2, and Fe_3O_4@mSiO_2@Au NPs in water dispersions was assessed using a dynamic light scattering (DLS) technique, revealing a size (i.e., hydrodynamic diameter) distribution peaked at about 8.1, 32.8, and 58.5 nm (Fig. 2a), which is consistent with the TEM results. The TEM and DLS results, along with absorbance spectrum of Au NPs dispersion are shown in Fig. S4. As it can be seen in

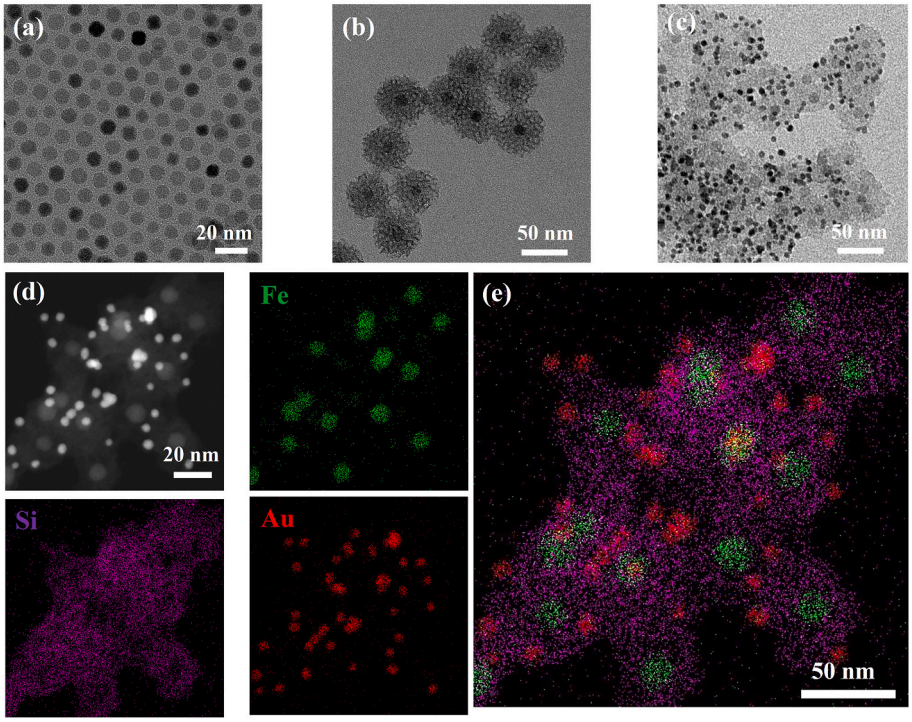

Fig. 1. TEM images of Fe_3O_4 NPs (a), Fe_3O_4@mSiO_2 NPs (b), Fe_3O_4@mSiO_2@Au NPs (c). (d) and (e): Elemental mappings showing the spatial distribution of Fe (green), Si (magenta), and Au (red) in the Fe_3O_4@mSiO_2@Au NPs.

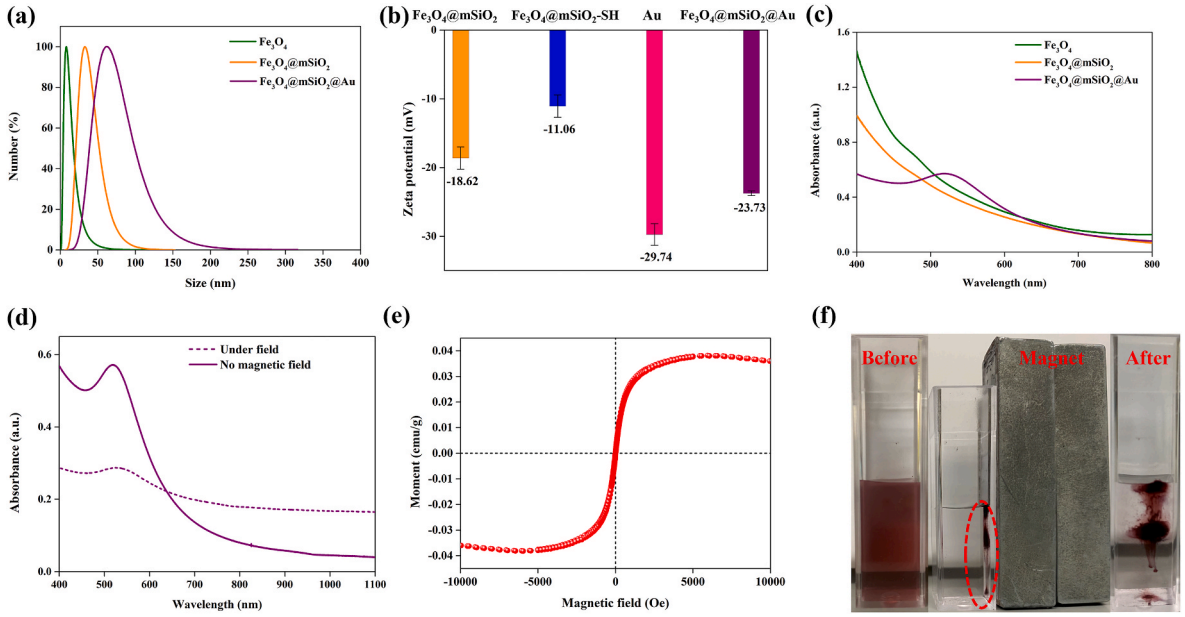

Fig. 2. (a) DLS data for Fe_3O_4, Fe_3O_4@mSiO_2 and Fe_3O_4@mSiO_2@Au NPs; (b) ζ potentials for Fe_3O_4@mSiO_2, MPTES-modified Fe_3O_4@mSiO_2, Au and Fe_3O_4@mSiO_2@Au NPs. (c) UV–Vis absorbance of Fe_3O_4, Fe_3O_4@mSiO_2, Fe_3O_4@mSiO_2@Au NPs. (d) Absorption spectra of Fe_3O_4@mSiO_2@Au NPs dispersion with and without applied MF. (e) Hysteresis loop and (f) visualization of the magnetophoretic response of the Fe_3O_4@mSiO_2@Au NPs.

Fig. 2b, the ζ potential of the Fe_3O_4@mSiO_2 NPs was found to change from −18.62 mV to −11.06 mV as a result of modification with MPTES; the following change of ζ potential from −11.06 mV to −23.73 mV is associated with the gold seeding (−29.74 mV) [57]. The UV–Vis absorbance spectra of Fe_3O_4, Fe_3O_4@mSiO_2 and Fe_3O_4@mSiO_2@Au NPs dispersions are shown in Fig. 2c. While the Fe_3O_4 and Fe_3O_4@mSiO_2 NPs display no absorption peak in the region of 400–1000 nm, Fe_3O_4@mSiO_2@Au NPs reveal the absorption band peaked at ~520 nm, which is evidently associated with gold satellites on the NPs surface. Furthermore, it was found that the absorption spectrum of core@shell@satellites NPs dispersion noticeably changed when MF was applied with the most significant change (i.e., appearance of the intense absorption without a pronounced peak) in the NIR spectral range (Fig. 2d). The magnetization of the Fe_3O_4@mSiO_2@Au NPs, which was measured with an applied magnetic field of up to 10000 Oe, shows saturation, but no hysteresis, revealing the superparamagnetic behavior

(Fig. 2e). At the same time, when the magnet was applied to the cuvette with the NPs dispersion, the NPs gathered on the inner wall of the cuvette (Fig. 2f). This type of NPs gathering evidently leads to a change (increase) in NIR absorption, which can be associated with a plasmon coupling effect produced by the Au nanoparticles becoming adjacent due to an MF-induced formation of Fe_3O_4@mSiO_2@Au NPs aggregates/clusters [29,35,58]. Fig. S6 shows data illustrating the formation of such NPs aggregates. The fact that the magnetically-activated formation of the Fe_3O_4@mSiO_2@Au aggregates leads to a significant increase in the NIR absorption can apparently lead to a possibility of MF-induced enhancement of NIR PT effect that, in turn, can be used for MF-enhanced NIR PTT of cancer.

3.2. Assessment of DOX loading and photothermal effect

At the next stage of our studies, we explored loading of DOX molecules to the mesoporous silica shell of NPs [48]. As a result of loading, ζ potential of NPs changed from −23.73 mV (for Fe_3O_4@mSiO_2@Au NPs, Fig. 2b) to −9.18 mV (for Fe_3O_4@mSiO_2@Au-DOX, Fig. S7b). The size of Fe_3O_4@mSiO_2@Au-DOX NPs did not change significantly compared to the unloaded Fe_3O_4@mSiO_2@Au NPs, indicating the structure and morphology of magnetoplasmonic NPs was not affected, and the DOX loading capacity was determined to be ~39 % (Fig. S8). Furthermore, using DLS measurements, the colloidal stability of Fe_3O_4@mSiO_2@Au-DOX NPs under physiological conditions was evaluated when NPs were dispersed in deionized water, PBS (pH = 7.4), and DMEM. As it is shown in Fig. S9, though an increase of the hydrodynamic diameter of NPs in PBS and DMEM has been observed (which is evidently associated with a formation of a solvation shell in PBS and DMEM), no significant changes in size of Fe_3O_4@mSiO_2@Au-DOX NPs could be noticed after 5 days of storage, indicating good colloidal stability and storage ability of Fe_3O_4@mSiO_2@Au-DOX NPs.

Fig. 3(a–c) shows absorption and fluorescence spectra of Fe_3O_4@mSiO_2@Au NPs with and without DOX, as well as spectra of DOX in water and DMF solutions. Although absorption spectra do not clearly reveal entrapment of DOX by Fe_3O_4@mSiO_2@Au NPs (due to the dominating plasmonic absorption band of gold satellites), the presence of DOX in the NPs dispersion is confirmed by the DOX fluorescence manifested by Fe_3O_4@mSiO_2@Au-DOX NPs dispersion. Moreover, fluorescence of DOX loaded to Fe_3O_4@mSiO_2@Au NPs is highly anisotropic, in contrast to fluorescence of free DOX water and DMF solutions (Fig. 3c). This feature is highly characteristic and associated with the limitation of the rotational mobility of fluorescent molecules bound to NPs [59,60]. It was also found that the absorption spectrum of Fe_3O_4@mSiO_2@Au-DOX NPs dispersion noticeably changed when MF was applied with the most significant change (i.e., appearance of the

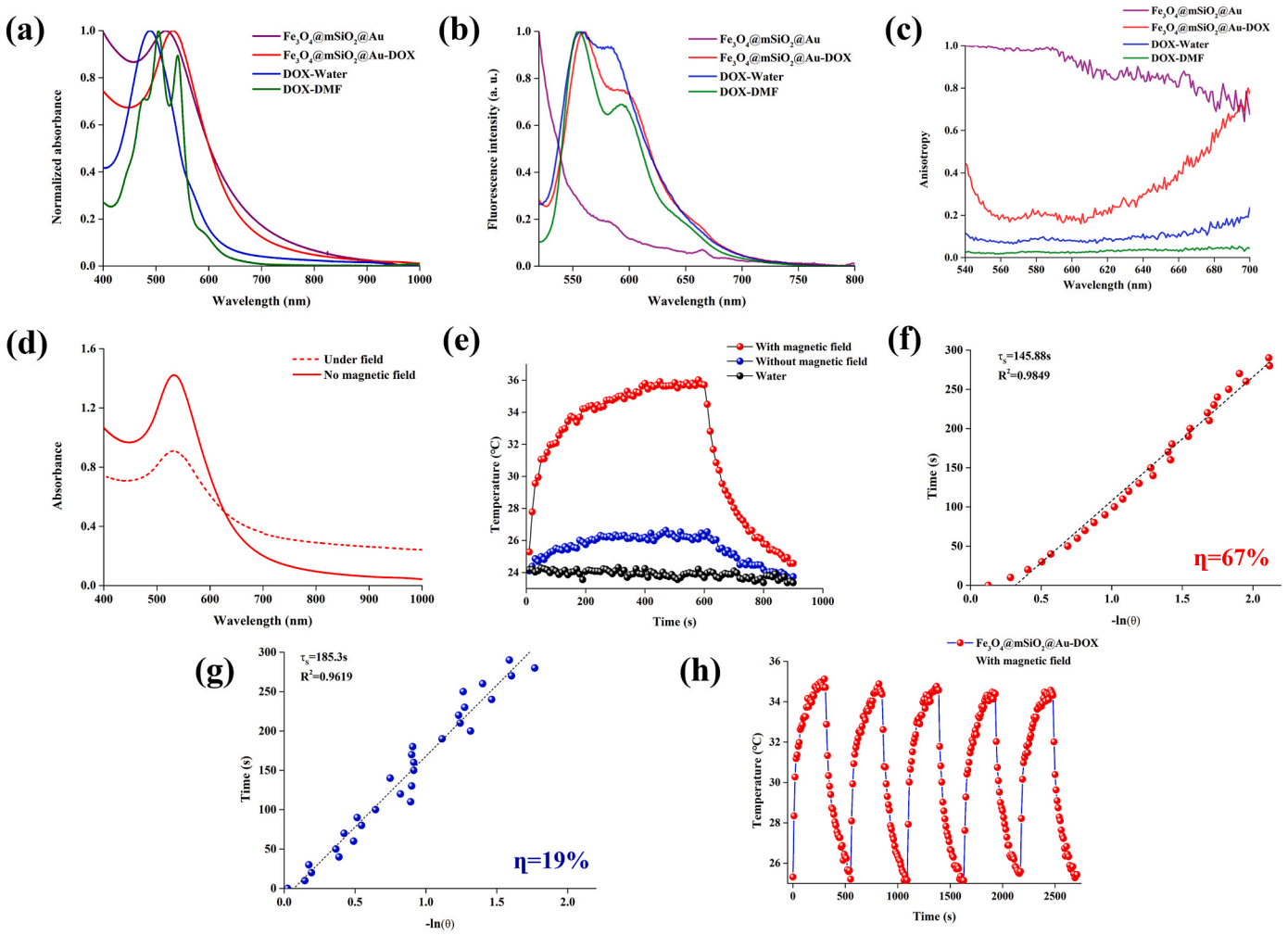

Fig. 3. (a–c) Spectra of UV–Vis absorption (a), fluorescence intensity (b), and fluorescence anisotropy (c) of Fe_3O_4@mSiO_2@Au and Fe_3O_4@mSiO_2@Au-DOX, and DOX solutions in water and DMF. (d) Absorbance of Fe_3O_4@mSiO_2@Au-DOX NPs dispersion with and without applied MF. (e) 808 nm laser induced heating and cooling of water (black curve) and Fe_3O_4@mSiO_2@Au-DOX water dispersion with (red) and without (blue) MF applied; (f–g) Dependence of cooling times on-ln(θ) obtained from the cooling stage for Fe_3O_4@mSiO_2@Au-DOX NPs dispersion with an applied MF. (h) Reproducibility of PT effect induced by irradiation with 808 nm laser (100 mW/cm^2) in Fe_3O_4@mSiO_2@Au-DOX NPs dispersion with an applied MF.

intense absorption without a pronounced peak) in NIR spectral range (Fig. 3d), demonstrating MF-induced the plasmon coupling effect produced by the Au nanoparticles was not affect even after DOX molecules loading.

As we observed the magnetically induced formation of the Fe_3O_4@$mSiO_2$@Au NPs aggregates that led to a significant increase in NIR absorption, we further suggested that this effect should result in MF-induced enhancement of NIR PT effect, which, in turn, can be used for MF-enhanced NIR PTT of cancer. To confirm that, we first explored changes in temperature of Fe_3O_4@$mSiO_2$@Au-DOX NPs dispersion with MF applied and without it, when the dispersion was irradiated with an 808 nm laser at different power densities. As shown in Fig. S10 (a), the temperature of the Fe_3O_4@$mSiO_2$@Au-DOX NPs dispersion in absence of MF remained unchanged under irradiation by 808 nm laser for all power densities used (i.e., 50, 100, 200 and 300 mW/cm^2). It should be also noted that in absence of MF the difference between temperature of the NPs dispersion and water was negligible for all laser power densities and the measured temperatures were in the same room temperature range (25 °C). In striking contrast, temperature of Fe_3O_4@$mSiO_2$@Au-DOX NPs dispersion in presence of MF noticeably rose even for the lowest irradiation power density of 50 mW/cm^2 and reached ~29 °C already ~40 s after the irradiation started, remaining approximately the same during the rest of the irradiation time (up to 300s). Under 808 nm laser irradiation with 100, 200 and 300 mW/cm^2, temperature of NPs dispersion under MF reached 34 °C, 38 °C and 43 °C, respectively. As shown in Fig. S10(b), temperature of the Fe_3O_4@$mSiO_2$@Au-DOX NPs dispersion gradually increased in presence of MF, and temperature of NPs dispersion under MF reached 30 °C, 35 °C, 40 °C, and 52 °C at different concentrations of NPs dispersion, respectively. Next, we have calculated PT conversion efficiency (η) of Fe_3O_4@$mSiO_2$@Au-DOX NPs dispersion with and without applied MF, using the absorption spectra of the NPs dispersion (with and without MF) and plots of its heating and cooling (Fig. 3d, e, 3f, 3g), along with appropriate equations, as described elsewhere (see the relevant section in Supporting information). The PT conversion efficiency was determined to be ~67 % and ~19 %, respectively, revealing a much better efficiency of the MF-induced Fe_3O_4@$mSiO_2$@Au-DOX aggregates in the conversion of 808 nm laser energy into heat. It should be noted that the PT conversion efficiency of MF-induced Fe_3O_4@$mSiO_2$@Au-DOX NPs aggregates has been found to be significantly higher than a majority of the previously reported PTT agents (Table S1, Supporting Information). As it is shown in Fig. 3h, the PT effect produced by Fe_3O_4@$mSiO_2$@Au-DOX in presence of MF manifests an excellent reproducibility under 808 nm laser irradiation, suggesting the stability of the Fe_3O_4@$mSiO_2$@Au-DOX aggregates under laser irradiation with power density of 100 mW/cm^2.

3.3. Magnetoplasmonic nanoparticles with cells in vitro

We have further studied an uptake of Fe_3O_4@$mSiO_2$@Au-DOX NPs by cancer cells *in vitro*. Fluorescence microscopy of the cells treated with Fe_3O_4@$mSiO_2$@Au-DOX NPs revealed a cytoplasmic localization of DOX fluorescence (Fig. 4a and b), in contrast to a nuclear localization of unbound DOX (Fig. S11), which is typical for free doxorubicin [60]. The observed cytoplasmic localization of fluorescence could be attributed to DOX associated with NPs even 12 h post cell treatment. It should be noted that after 6 h of treatment, fluorescence signal from cells with applied MF was found to be noticeably higher than that from cells in the absence of MF (Fig. 4a). This is understandable as magnetically attracted drug nanocarriers were known to allow for higher drug uptake by MF treated cells *in vitro* [22,29,61]. Furthermore, the DOX fluorescence signal from the cells in the absence of MF did not noticeably increase after laser irradiation followed by 6 more h of incubation, whereas it did significantly rise 6 h post laser irradiation in case of the cells with applied MF (Fig. 4b–Fig. S12). The latter suggests that while the MF application is a major reason causing increase in DOX delivery with Fe_3O_4@$mSiO_2$@Au-DOX NPs, laser irradiation might also be a factor here, increasing cellular uptake through a mild PT effect. At the same time, laser irradiation with the applied parameters (10 min, 100 mW/cm^2) did not noticeably affect the viability of the imaged cells.

The viability of the NPs treated cells was further evaluated using CCK-8 assay. As shown in Fig. 4c, the viability of non-irradiated HeLa cells treated with Fe_3O_4@$mSiO_2$@Au NPs at a concentration of 50 μg/mL remained about 100 % both in the presence of MF and without it. The cell viability was slightly decreased for the cells treated with Fe_3O_4@$mSiO_2$@Au-DOX NPs in the absence of MF and it was noticeably reduced when MF was applied, which is evidently associated with an increase in DOX uptake. Furthermore, the viability of the 808 nm laser irradiated (100 mW/cm^2) cells treated with Fe_3O_4@$mSiO_2$@Au and Fe_3O_4@$mSiO_2$@Au-DOX NPs with and without MF application was accessed (Fig. 4d, e, 4f). As one can see, similarly to non-irradiated cells, the cytotoxicity of Fe_3O_4@$mSiO_2$@Au-DOX NPs with the applied MF was stronger than that of Fe_3O_4@$mSiO_2$@Au NPs, which is apparently associated with the facilitated intracellular DOX accumulation and corresponding toxicity [62]. Moreover, cells treated with Fe_3O_4@$mSiO_2$@Au-DOX NPs in the presence of MF have shown a lowest viability after 808 nm laser irradiation compared to other cells (~32 % for 30 min of irradiation). This suggests that the external MF application following the injection of Fe_3O_4@$mSiO_2$@Au-DOX NPs into *in vivo* cancer model

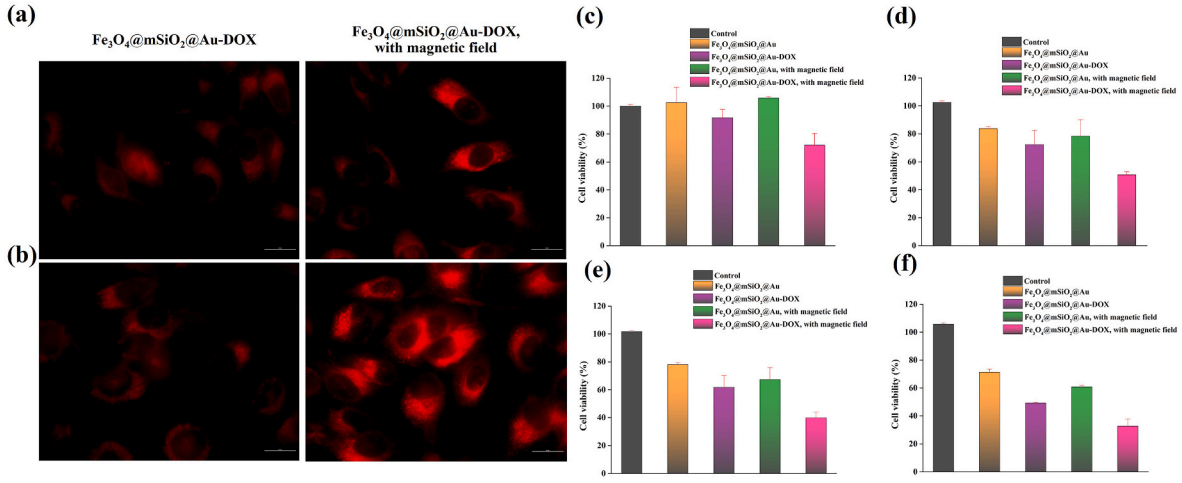

Fig. 4. (a, b). Fluorescence microscopy images of HeLa cells treated with Fe_3O_4@$mSiO_2$@Au-DOX NPs 6 h after treatment and before laser irradiation (a) and 12 h after treatment and 6 h after 808 nm laser irradiation (10 min, 100 mW/cm^2) (b). Scale bar is 25 μm. (c): Viability of the cells after different treatments without 808 nm laser irradiation. (d–f): Viability of the treated cells after 808 nm laser irradiation of the same power density (100 mW/cm^2) for 10, 20, and 30 min intervals.

can induce the formation of NPs aggregates in tumor in situ, leading to an enhanced therapeutic effect of PT/chemotherapy combination.

3.4. *In vivo* studies

The PT effect induced by magnetoplasmonic NPs and 808 nm laser irradiation was evaluated *in vivo* using 4T1 tumor-bearing mice. We randomly divided all mice into five groups (five mice each), which were given the following treatments: (1) intratumoral injection of PBS + 808 nm laser irradiation of a tumor; (2) intratumoral injection of Fe_3O_4@mSiO_2@Au NPs + 808 nm laser irradiation of a tumor; (3) intratumoral injection of Fe_3O_4@mSiO_2@Au-DOX NPs + 808 nm laser irradiation of a tumor; (4) intratumoral injection of Fe_3O_4@mSiO_2@Au NPs + MF application + 808 nm laser irradiation of a tumor; (5) intratumoral injection of Fe_3O_4@mSiO_2@Au-DOX NPs + MF application + 808 nm laser irradiation of a tumor. For the MF-treated groups 4 and 5, an external magnet was fixed on top of the tumor (using stick tape) immediately after injection and left there for 3 h. After magnet removal, a difference in color between MF-treated and MF-untreated tumors became visible, evidently originating from a magnetophoretically concentrated magnetoplasmonic NPs (Fig. S13). Three hours after injections, the tumors of mice from all groups were irradiated with 808 nm laser (300 mW/cm^2) for 20 min. The temperature changes during the irradiation were imaged using a thermal imaging camera. As shown in Fig. 5, temperature of the irradiated site (tumor) for mouse from group 1 slightly increased from 31 °C to 33 °C, while temperatures of the irradiated tumor rose a little more (from 31 °C to 35 °C) for mice from group 2 and 3. These results indicate that the irradiation by 808 nm laser with a power density of 300 mW/cm^2 do not overheat the irradiation sites in mice injected with PBS or with NPs (Fe_3O_4@mSiO_2@Au or Fe_3O_4@mSiO_2@Au-DOX). In stark contrast, the temperature at the irradiated tumor sites on the group 4 and 5-treated mice rapidly increased from 32 °C to 45 °C and 31 °C–46 °C, respectively, manifesting an enhanced NIR PT effect caused by MF induced aggregation of Fe_3O_4@mSiO_2@Au and Fe_3O_4@mSiO_2@Au-DOX magnetoplasmonic NPs.

Along with the evaluation of the MF induced NIR PT effect, the efficiency of the combined antitumor therapy was assessed *in vivo* using the same groups of 4T1 tumor-bearing mice (1–5). The general scheme of the therapy including a tumor model establishment and the treatment evaluations is illustrated in Fig. 6a. As it can be seen in the scheme, on the tenth day after cancer cell inoculation, tumors of the group 1–5 were injected and the evaluation of the NIR PT effect was performed as described above (Fig. 5). Next day, tumors in the mice of the groups 1–5 were again irradiated by 808 nm laser and tumor developments were evaluated for 9 more days to determine the antitumor ability of the treatment. The body weights and tumor volumes were measured every day until tenth day since the treatment began. It is worth also noting that the body weight in all groups did not noticeably changed during the *in vivo* studies (Fig. 6b). At the same time, as shown in Fig. 6b, rapid tumor growth was observed in the group 1 (PBS) and group 2 (Fe_3O_4@mSiO_2@Au NPs), indicating a negligible antitumor effect in these two groups due to an absence of the chemotherapy and NIR PTT. Both group 3 (Fe_3O_4@mSiO_2@Au-DOX NPs + laser) and group 4 (Fe_3O_4@mSiO_2@Au NPs + MF + laser) somewhat slowed down the tumor development, due to the chemotherapeutic and NIR PTT effects, correspondingly. Notably, group 5 (Fe_3O_4@mSiO_2@Au-DOX NPs + MF + laser) manifested the most significantly suppressed tumor growth. Thus, the combination of MF-induced NIR PTT and chemotherapy delivered with Fe_3O_4@mSiO_2@Au-DOX synergistically enhanced the antitumor therapy efficiency. The representative photographs of tumors harvested from mice in groups 1–5 on 10th day after first treatment (Fig. S14), results on tumor growth inhibition (Fig. S15) and final tumor weight (Fig. 6c) additionally highlight a superior tumor-inhibiting effect arising from a combination of an MF-induced NIR PTT and chemotherapy produced magnetoplasmonic nanoplatform loaded with chemotherapeutics.

The achieved therapeutic effect was further assessed using histological studies (H&E staining) of the tumor tissues collected at the end of the experiment (Fig. 6d, e, 6f, 6g, 6h). The histological examination of the collected specimen revealed a high level of cell polymorphism in all groups. At the same time, both group 1 (PBS + laser) and group 2 (Fe_3O_4@mSiO_2@Au NPs + laser) tumors demonstrated similar histological characteristics with prominent signs of malignancy. The tumors from group 3 (Fe_3O_4@mSiO_2@Au-DOX NPs + laser) and group 4 (Fe_3O_4@mSiO_2@Au NPs + MF + laser) are still similar, but have fewer signs of malignancy. The tumor tissue from group 5 (Fe_3O_4@mSiO_2@Au-DOX NPs + MF + laser) is very different from others, displaying the lowest degree of tumor development and malignancy, as it can be concluded from the observed pathological changes. In particular, the total hyperchromicity in the tumor cell nuclei is reduced for groups 3, 4 and 5 in comparison with those from groups 1 and 2 (a more intensive basophilic cell staining, predominantly due to nucleus/chromatin, is a common sign of tumor progression [63]). Next, the number of mitotic cells per 1 mm^2, counted at the tumor periphery (Fig. 6i), decreased in the groups as followed: 65 (group 1) > 52 (group 2) > 41 (group 3) ≈ 43 (group 4) > 19 (group 5). Furthermore, many cancer-associated fibroblasts (which form the extracellular matrix and tumor stroma) were found in the specimen from the groups 1–4. It should be noted that the process of fibrosis contributes to the tumor progression by maintaining its structure and supplying signaling molecules, as well as by providing a pool of mobile cells, which increase metastatic potential, and supporting areas of inflammation [64,65]. This process is most clearly observed in groups 1 and 2 (a relative fibrosis area is of ~25 %) and in groups 3 and 4 (a 19–20 % fibrosis).

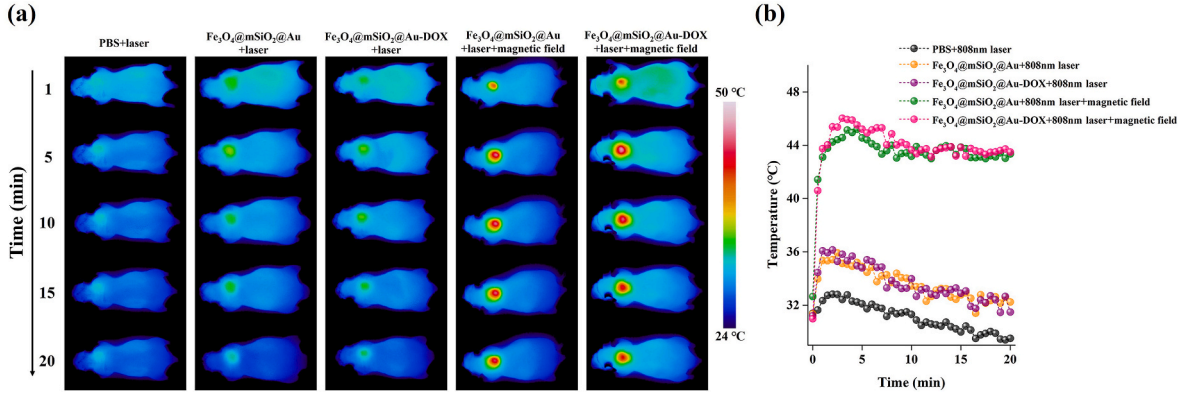

Fig. 5. *In vivo* NIR PT effect. (a) Thermal images and (b) temperature changes of 4T1 tumor-bear mice under the 808 nm laser irradiation (300 mW/cm^2 for 20 min). Mice were treated with: PBS (1), Fe_3O_4@mSiO_2@Au NPs (2), Fe_3O_4@mSiO_2@Au-DOX NPs (3), Fe_3O_4@mSiO_2@Au NPs + MF (4), and Fe_3O_4@mSiO_2@Au-DOX NPs + MF (5).

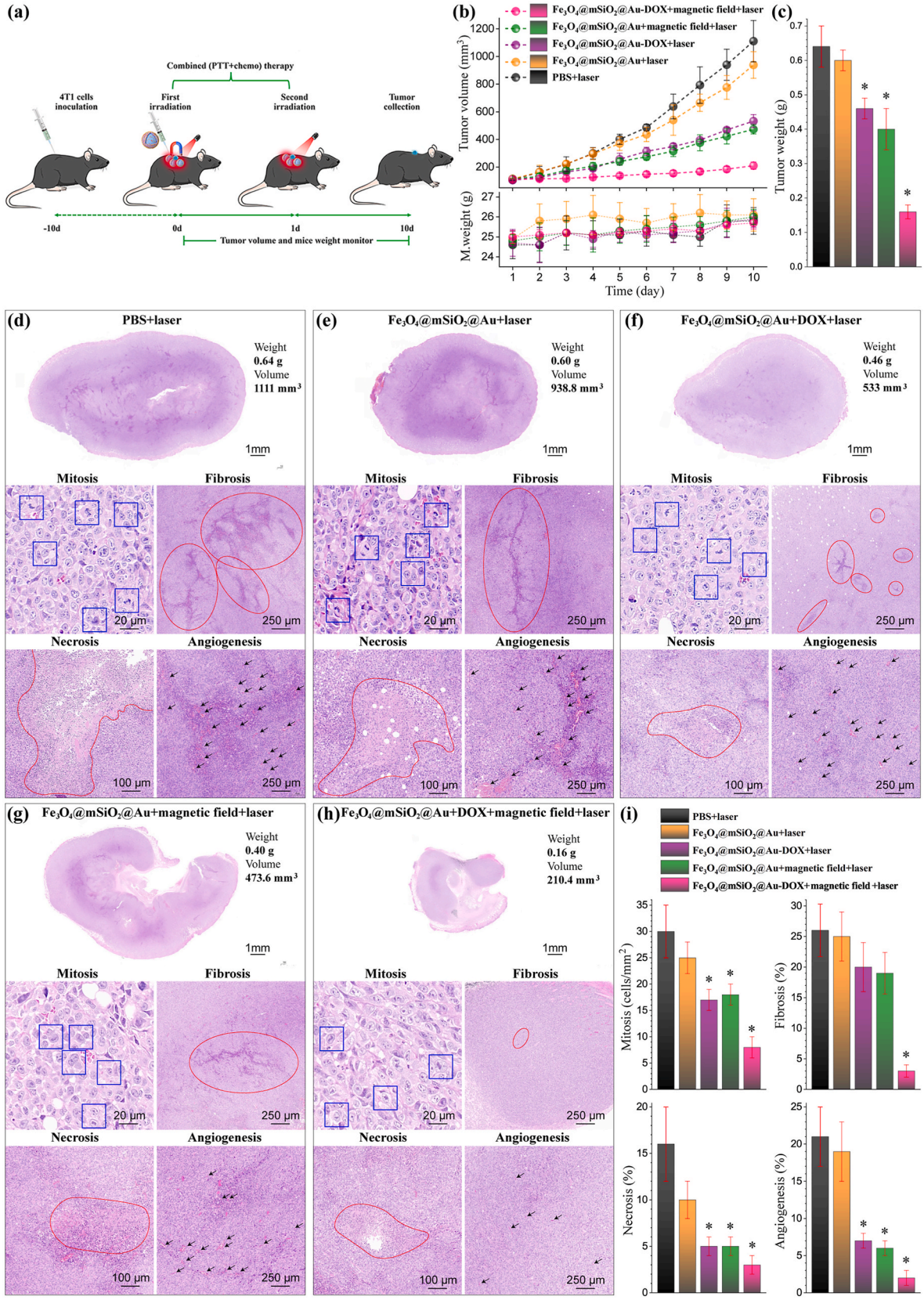

Fig. 6. (a) Scheme illustrating tumor generation in mice *in vivo* and tumor treatment by combination of MF-induced NIR PTT and chemotherapy. (b) Changes of tumor volumes and body weights for mice in groups (1–5), measured daily. (c) Tumor weights measured after collection on 10th day post injection. (d–h) H&E-stained histological images of tumor tissues from each group: (d) group 1 (PBS + laser), (e) group 2 (Fe_3O_4@mSiO_2@Au NPs + laser), (f) group 3 (Fe_3O_4@m-SiO_2@Au-DOX NPs + laser), (g) group 4 (Fe_3O_4@mSiO_2@Au NPs + MF + laser), and (h) group 5 (Fe_3O_4@mSiO_2@Au-DOX NPs + MF + laser). (i) Mitosis, fibrosis, necrosis and hematopoiesis in tumors from groups (1–5). The data are presented as mean ± SD (n = 3), *p < 0.05 for data with a statistically significant difference.

Remarkably, fibrosis has been drastically suppressed down to 3 % in group 5 (Fig. 6i). The relative areas of necrosis were measured to be 16 and 10 % in group 1 and group 2 tumor specimen; necrotic sites appeared to be smaller in the tumor tissue from group 2. In the tumor tissues from other group, the area of necrosis was much smaller (~3 % of the total area); necrotic sites were small in size, not as pronounced, and single in number (Fig. 6i). A few typical provascular structures were observed in the specimens from groups 1 and 2. Moreover, signs that could be attributed to extramedullary tumor hematopoiesis were well manifested in these groups. It should be noted that the process of hematopoiesis in tumors includes the formation of erythroid and myeloid progenitor cells, which then differentiate to blood cells [66,67]. This process maintains oncoangiogenesis, plays an important role in the disruption of anti-tumor immunity and supports cancer aggressiveness [68]. The signs of hematopoiesis (Fig. 6d–i and Fig. S16) are clearly seen in the tumors from group 1 (21 %) and group 2 (19 %), while they are noticeably depressed in group 3 (7 %) and group 4 (6 %) and almost completely disappear in the specimen from group 5 (2 %).

3.5. Effect of treatments on metastasis and biocompatibility of Fe_3O_4@mSiO$_2$@Au-DOX nanoparticles

As the majority of deaths associated with cancer are due to the metastasis of primary tumor cells, an inhibition of metastasis can be considered as an extremely important outcome of cancer therapy. Therefore, the main organs (i.e., lungs, liver, spleen and kidneys) of mice in groups (1–5) were histologically analyzed for the presence of metastases. The study of specimens of lungs and liver from group 1 mice revealed the largest (from all groups) average number of metastases (5 and 10 per mm^2, respectively), and also inflammatory processes in the lungs, which can be precancerous areas (Fig. 7a and f). For the mice from groups 2 and 4, the average number of metastases was found to be the same (2 and 8.5 per mm^2) in the specimens from lungs and liver tissues, respectively (Fig. 7b, d, 7f). Interestingly enough, tissue specimens from group 3 contained even less metastases; the average number of metastases was 1.5 and 4 per mm^2 for lungs and liver, respectively (Fig. 7c and f). However, the specimens from group 5 manifested the very least average number of metastasis: 0.1 and 1 per mm^2 for lungs and liver, respectively (Fig. 7d and f). At the same time, no metastases were found in the spleen and kidneys of mice from all the groups (Fig. 7).

In addition to the evaluation of the cancer treatment efficiency, it is essential to assess the systemic safety of the nanoformulations and the associated therapeutic approach. Therefore, the toxicity of the applied treatments was evaluated not only *in vivo* using mice body weight measurements (Fig. 6b), but also *ex vivo* (by routine blood analysis, and H&E staining of the collected tissue samples). Neither damages or inflammatory lesions were observed in the assessed organs (liver, kidney, spleen, and lungs), implying low systemic toxicity of Fe_3O_4@mSiO$_2$@Au-DOX NPs and the proposed treatment strategy (Fig. 7). The main hematology indicators for blood with Fe_3O_4@mSiO$_2$@Au-DOX

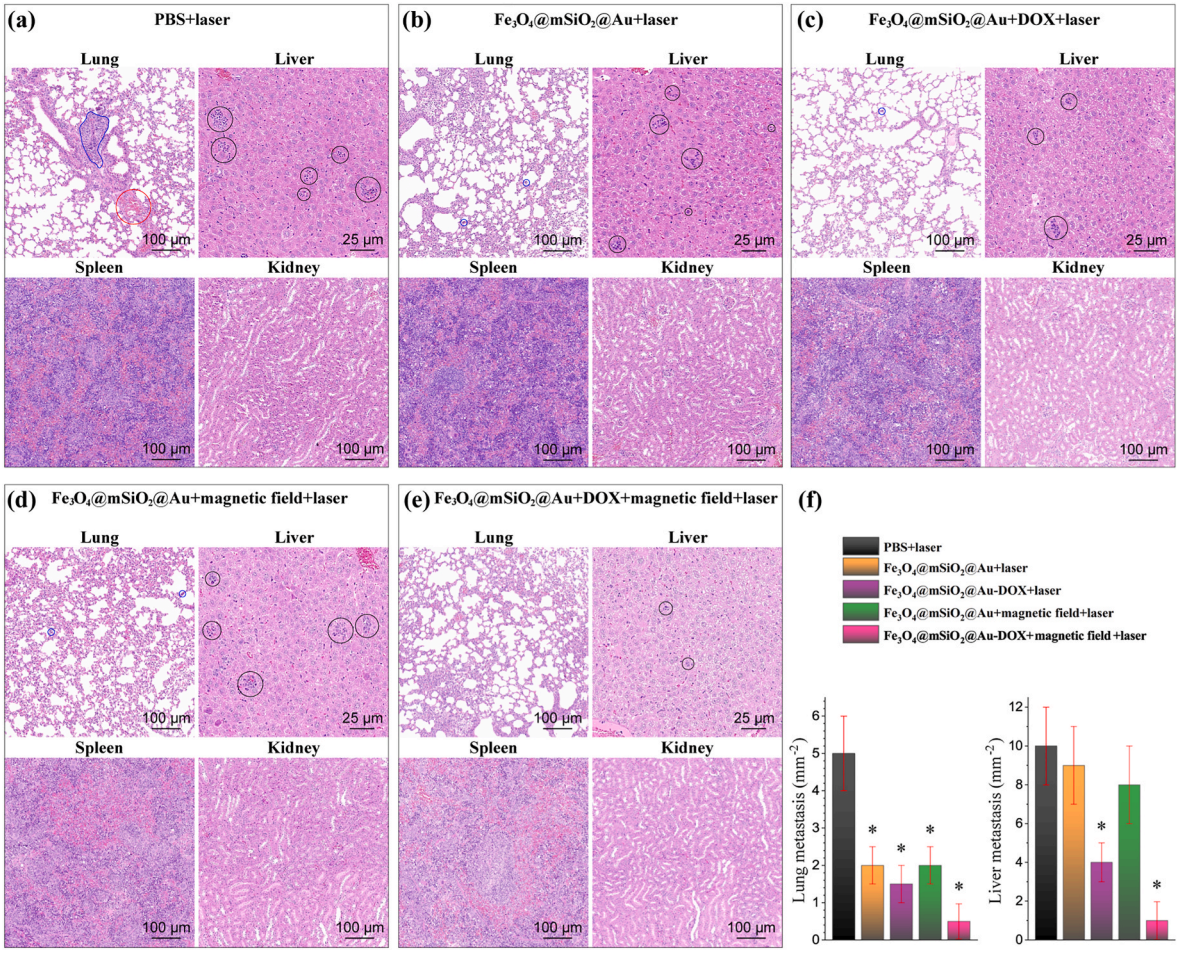

Fig. 7. H&E-stained histological images of tissues from lungs, liver, spleen and kidneys to evaluate physiological changes and presence of metastasis in mice from different groups. (a): group 1 (PBS + laser), (b): group 2 (Fe_3O_4@mSiO$_2$@Au NPs + laser), (c): group 3 (Fe_3O_4@mSiO$_2$@Au-DOX NPs + laser), (d): group 4 (Fe_3O_4@mSiO$_2$@Au NPs + MF + laser), (e): group 5 (Fe_3O_4@mSiO$_2$@Au-DOX NPs + MF + laser). Red circle shows the inflammation area, blue circles and outlined area show the lung metastases, black circles show the liver metastases. (f) Number of the lung and liver metastases in each group. The data are presented as mean ± SD (n = 3), *p < 0.05 for data with a statistically significant difference.

NPs in circulation were then analyzed (Fig. S17). Similar blood parameters were obtained for all five groups, further demonstrating good biocompatibility of Fe_3O_4@mSiO_2@Au-DOX NPs and the treatment strategy. These results confirmed that Fe_3O_4@mSiO_2@Au magnetoplasmonic NPs loaded with chemotherapeutic drug is a promising nanoplatform that can be employed to achieve magnetic field-enhanced, synergistic cancer therapy.

4. Conclusions

In conclusion, this study introduces a cancer treatment using a magnetic field-induced and targeted combination of near-infrared photothermal therapy (NIR PTT) and chemotherapy utilizing Fe_3O_4@mSiO_2@Au core@shell@satellites nanoparticles (NPs) loaded with the chemotherapeutic drug doxorubicin. When an external magnetic field (MF) is applied to the dispersion of these NPs, it results in the magnetophoretic movement and aggregation of the NPs. This aggregation leads to notable absorption in NIR spectral range, due to plasmon resonance coupling between the Au NPs within the aggregates. Additionally, the MF-induced aggregates reveal increased photothermal conversion efficiency. As a result, an enhanced photothermal effect is observed in MF-treated NP dispersion under 808 nm laser irradiation. This MF-delivered, tumor targeted combination of NIR PTT with DOX chemotherapeutic action effectively kills cancer cells *in vitro* and restricts tumor growth in 4T1-tumor-bearing mice *in vivo*. Histological studies of the tumor tissues show significant differences in the development and malignancy between tumors treated with the Fe_3O_4@mSiO_2@Au-DOX NPs, MF application, and 808 nm laser irradiation, compared to control treatments. These differences, including mitosis of cancer cells in the treated tumor tissues along with the tissue fibrosis, necrosis, hematopoiesis, and metastasis, highlight the synergy between MF-induced NIR PTT and DOX chemotherapy delivered with the magnetoplasmonic nanoplatform. Based on the obtained results, we suggest an efficient strategy that integrates MF-induced PTT and targeted drug delivery. Our study revealed and exploited strong enhancement of NIR absorption of the magnetopasmonic NPs, which appeared only under the external magnetic field but not without it. Thus, this approach allows for additional therapeutic selectivity: MF localized NIR plasmonic absorption, correspondent selectively localized NIR PTT and, synergistically enhanced, targeted cancer therapy.

CRediT authorship contribution statement

Siqi Gao: Writing – original draft, Investigation, Formal analysis, Data curation. **Iuliia Golovynska:** Writing – original draft, Investigation, Data curation. **Jiantao Liu:** Validation, Investigation, Data curation. **Zhenlong Huang:** Investigation, Data curation. **Hao Xu:** Validation, Investigation. **Jinghan Qu:** Investigation. **Fangrui Lin:** Investigation. **Galyna Ostrovska:** Data curation. **Junle Qu:** Writing – review & editing, Project administration, Funding acquisition. **Tymish Y. Ohulchanskyy:** Conceptualization, Writing – review & editing, Supervision, Project Administration, Methodology, Investigation, Funding acquisition.

Declaration of competing interest

The authors declare that they have no known competing financial interests or personal relationships that could have appeared to influence the work reported in this paper.

Acknowledgements

This work has been partially supported by the National Natural Science Foundation of China (62361136586/T2421003/62127819/61875135; Shenzhen Key Laboratory of Photonics and Biophotonics (ZDSYS20210623092006020) and Shenzhen Science and Technology Program (JCYJ20220818100202005, JCYJ20170818090620324).

Appendix A. Supplementary data

Supplementary data to this article can be found online at https://doi.org/10.1016/j.mtbio.2024.101393.

Data availability

Data will be made available on request.

References

[1] F. Bray, J. Ferlay, I. Soerjomataram, R.L. Siegel, L.A. Torre, A. Jemal, Global cancer statistics 2018: GLOBOCAN estimates of incidence and mortality worldwide for 36 cancers in 185 countries, CA A Cancer J. Clin. 68 (6) (2018) 394–424.
[2] R.L. Sabado, S. Balan, N. Bhardwaj, Dendritic cell-based immunotherapy, Cell Res. 27 (2017) 74–95.
[3] Z. Karjoo, X. Chen, A. Hatefi, Progress and problems with the use of suicide genes for targeted cancer therapy, Adv. Drug Deliv. Rev. 99 (2016) 113–128.
[4] P.M. Costa, A.L. Cardoso, C. Custódia, P. Cunha, L.P. Almeida, M.C.P. Lima, MiRNA-21 silencing mediated by tumor-targeted nanoparticles combined with sunitinib: a new multimodal gene therapy approach for glioblastoma, J. Contr. Release 207 (2015) 31–39.
[5] R. Zhao, X. Liu, X. Yang, B. Jin, C. Shao, W. Kang, R. Tang, Nanomaterial-based organelles protect normal cells against chemotherapy-induced cytotoxicity, Adv. Mater. 30 (27) (2018) 1801304.
[6] W. Wang, C. Hao, M. Sun, L. Xu, C. Xu, H. Kuang, Spiky Fe_3O_4@Au supraparticles for multimodal in vivo imaging, Adv. Funct. Mater. 28 (22) (2018) 1800310.
[7] A. Naik, R. Rubbiani, G. Gasser, B. Spingler, Visible-light-induced annihilation of tumor cells with platinum-porphyrin conjugates, Angew. Chem., Int. Ed. 126 (27) (2014) 7058–7061.
[8] S. Li, W. Zhang, R. Xing, C. Yuan, H. Xue, X. Yan, Supramolecular nanofibrils formed by coassembly of clinically approved drugs for tumor photothermal immunotherapy, Adv. Mater. 33 (29) (2021) 2103733.
[9] R. Han, Y. Xiao, Q. Yang, M. Pan, Y. Hao, X. He, J. Peng, Z. Qian, Ag_2S nanoparticle-mediated multiple ablations reinvigorates the immune response for enhanced cancer photo-immunotherapy, Biomaterials 264 (2021) 120451.
[10] L. Cheng, W. He, H. Gong, C. Wang, Q. Chen, Z. Cheng, Z. Liu, PEGylated micelle nanoparticles encapsulating a non-fluorescent near-infrared organic dye as a safe and highly-effective photothermal agent for in vivo cancer therapy, Adv. Funct. Mater. 23 (47) (2013) 5893–5902.
[11] Q. Zou, M. Abbas, L. Zhao, S. Li, G. Shen, X. Yan, Biological photothermal nanodots based on self-assembly of peptide-porphyrin conjugates for antitumor therapy, J. Am. Chem. Soc. 139 (5) (2017) 1921–1927.
[12] M. Overchuk, R.A. Weersink, B.C. Wilson, G. Zheng, Photodynamic and photothermal therapies: synergy opportunities for nanomedicine, ACS Nano 17 (9) (2023) 7979–8003.
[13] A.G. Van der Heijden, M.W. Dewhirst, Effects of hyperthermia in neutralising mechanisms of drug resistance in non-muscle-invasive bladder cancer, Int. J. Hyperther. 32 (4) (2016) 434–445.
[14] N. Borys, M.W. Dewhirst, Drug development of lyso-thermosensitive liposomal doxorubicin: combining hyperthermia and thermosensitive drug delivery, Adv. Drug Deliv. Rev. 178 (2021) 113985.
[15] M. Khafaji, M. Zamani, M. Golizadeh, O. Bavi, Inorganic nanomaterials for chemo/photothermal therapy: a promising horizon on effective cancer treatment, Biophys. Rev. 11 (2019) 335–352.
[16] G. Yang, R. Lv, F. He, F. Qu, S. Gai, S. Du, Z. Wei, P. Yang, A core/shell/satellite anticancer platform for 808 NIR light-driven multimodal imaging and combined chemo-/photothermal therapy, Nanoscale 7 (2015) 13747–13758.
[17] X. Song, W. Fu, U.K. Cheang, Immunomodulation and delivery of macrophages using nano-smooth drug-loaded magnetic microrobots for dual targeting cancer therapy, iScience 25 (7) (2022) 104507.
[18] V. Karthika, M.S. AlSalhi, S. Devanesan, K. Gopinath, A. Arumugam, M. Govindarajan, Chitosan overlaid Fe_3O_4/rGO nanocomposite for targeted drug delivery, imaging, and biomedical applications, Sci. Rep. 10 (2020) 18912.
[19] H. Lu, Y. Xu, R. Qiao, Z. Lu, P. Wang, X. Zhang, A. Chen, L. Zou, Z. Wang, A novel clustered SPIO nanoplatform with enhanced magnetic resonance T2 relaxation rate for micro-tumor detection and photothermal synergistic therapy, Nano Res. 13 (2020) 2216–2225.
[20] M. Saadat, M.K.D. Manshadi, M. Mohammadi, M.J. Zare, M. Zarei, R. Kamali, A. Sanati-Nezhad, Magnetic particle targeting for diagnosis and therapy of lung cancers, J. Contr. Release 328 (2020) 776–791.
[21] O.A. Mayorova, O.A. Sindeeva, M.V. Lomova, O.I. Gusliakova, Y. V. Tarakanchikova, E.V. Tyutyaev, S.I. Pinyaev, O.A. Kulikov, S.V. German, N. A. Pyataev, D.A. Gorin, G.B. Sukhorukov, Endovascular addressing improves the effectiveness of magnetic targeting of drug carrier. Comparison with the conventional administration method, Nanomed-Nanotechnol 28 (2020) 102184.
[22] L.O. Cinteza, T.Y. Ohulchanskyy, S. Yudhisthira, J.B. Earl, K.P. Ravindra, N. P. Paras, Diacyllipid micelle-based nanocarrier for magnetically guided delivery of drugs in photodynamic therapy, Mol. Pharm. 3 (4) (2006) 415–423.

[23] Y. Li, J. Kong, H. Zhao, Y. Liu, Synthesis of multi-stimuli responsive Fe_3O_4 coated with diamonds nanocomposite for magnetic assisted chemo-photothermal therapy, Molecules 28 (4) (2023) 1784.
[24] T.T. Nguyen, F. Mammeri, S. Ammar, Iron oxide and gold based magneto-plasmonic nanostructures for medical applications: a review, Nanomaterials 8 (3) (2018) 149.
[25] B. Muzzi, M. Albino, A. Gabbani, A. Omelyanchik, E. Kozenkova, M. Petrecca, C. Innocenti, E. Balica, A. Lavacchi, F. Scavone, C. Anceschi, G. Petrucci, A. Ibarra, A. Laurenzana, F. Pineider, V. Rodionova, C. Sangregorio, Star-shaped magnetic-plasmonic $Au@Fe_3O_4$ nano-heterostructures for photothermal therapy, ACS Appl. Mater. Interfaces 14 (25) (2022) 29087–29098.
[26] Y. Gao, Y. Li, J. Chen, D. Zhu, X. Liu, L. Zhou, P. Shi, D. Niu, J. Gu, J. Shi, Multifunctional gold nanostar-based nanocomposite: synthesis and application for noninvasive MR-SERS imaging-guided photothermal ablation, Biomaterials 60 (2015) 31–41.
[27] J. Li, Y. Hu, J. Yang, P. Wei, W. Sun, M. Shen, G. Zhang, X. Shi, Hyaluronic acid-modified Fe_3O_4@ Au core/shell nanostars for multimodal imaging and photothermal therapy of tumors, Abstr. Pap. Am. Chem. Soc. 249 (2015) 276.
[28] L. Wang, D. Meng, Y. Hao, Y. Hu, M. Niu, C. Zheng, Y. Yin, D. Li, P. Zhang, J. Chang, Z. Zhang, Y. Zhang, A gold nanostar based multi-functional tumor-targeting nanoplatform for tumor theranostic applications, J. Mater. Chem. B 4 (2016) 5895–5906.
[29] T.Y. Ohulchanskyy, A. Kopwitthaya, M. Jeon, M. Guo, W.C. Law, E.P. Furlani, C. Kim, P.N. Prasad, Phospholipid micelle-based magneto-plasmonic nanoformulation for magnetic field-directed, imaging-guided photo-induced cancer therapy, Nanomed-Nanotechnol 9 (8) (2013) 1192–1202.
[30] A. Espinosa, J. Reguera, A. Curcio, A. Muñoz-Noval, C. Kuttner, A. van de Walle, L. M. Liz-Marzan, C. Wilhelm, Janus magnetic-plasmonic nanoparticles for magnetically guided and thermally activated cancer therapy, Small 16 (11) (2020) 1904960.
[31] P. Guardia, S. Nitti, M.E. Materia, G. Pugliese, N. Yaacoub, J.M. Greneche, C. Lefevre, L. Manna, T. Pellegrino, Gold–iron oxide dimers for magnetic hyperthermia: the key role of chloride ions in the synthesis to boost the heating efficiency, J. Mater. Chem. B 5 (2017) 4587–4594.
[32] M. Rincón-Iglesias, I. Rodrigo, L.B. Berganza, E.S. Abu Serea, F. Plazaola, S. Lanceros-Méndez, E. Lizundia, J. Reguera, Core-shell Fe_3O_4@Au nanorod-loaded gels for tunable and anisotropic magneto- and photothermia, ACS Appl. Mater. Interfaces 14 (5) (2022) 7130–7140.
[33] W. Li, P. Liao, C. Su, C. Yeh, Formation of oligonucleotide-gated silica shell-coated Fe_3O_4-Au core-shell nanotrisoctahedra for magnetically targeted and near-infrared light-responsive theranostic platform, J. Am. Chem. Soc. 136 (28) (2014) 10062–10075.
[34] Y. Zhang, T. Zhou, J. Li, N. Xu, M. Cai, H. Zhang, Q. Zhao, S. Wang, Au catalyzing control release NO in vivo and tumor growth-inhibiting effect in chemo-photothermal combination therapy, Int. J. Nanomed. 16 (2021) 2501–2513.
[35] I. Mukha, O. Chepurna, N. Vityuk, A. Khodko, L. Storozhuk, V. Dzhagan, D.R. T. Zahn, V. Ntziachristos, A. Chmyrov, T.Y. Ohulchanskyy, Multifunctional magneto-plasmonic Fe_3O_4/Au nanocomposites: approaching magnetophoretically-enhanced photothermal therapy, Nanomaterials 11 (5) (2021) 1113.
[36] F. Lu, A. Popa, S. Zhou, J. Zhu, A.C.S. Samia, Iron oxide-loaded hollow mesoporous silica nanocapsules for controlled drug release and hyperthermia, Chem. Commun. 49 (2013) 11436–11438.
[37] S. Gao, R. Zhou, S. Samanta, J. Qu, T.Y. Ohulchanskyy, Recent advances in plasmon-enhanced luminescence for biosensing and bioimaging, Anal. Chim. Acta 1254 (2023) 341086.
[38] Y. Hang, J. Boryczka, N. Wu, Visible-light and near-infrared fluorescence and surface-enhanced Raman scattering point-of-care sensing and bio-imaging: a review, Chem. Soc. Rev. 51 (2022) 329–375.
[39] Y. Zhang, P.M. Radjenovic, X. Zhou, H. Zhang, J. Yao, J. Li, Plasmonic core–shell nanomaterials and their applications in spectroscopies, Adv. Mater. 33 (50) (2021) 2005900.
[40] Y. Liu, Y. Liang, P. Lei, Z. Zhang, Y. Chen, Multifunctional superparticles for magnetically targeted NIR-II imaging and photodynamic therapy, Adv. Sci. 10 (2023) 202203669.
[41] J. Kim, H.S. Kim, N. Lee, T. Kim, H. Kim, T. Yu, I.C. Song, W.K. Moon, T. Hyeon, Multifunctional uniform nanoparticles composed of a magnetite nanocrystal core and a mesoporous silica shell for magnetic resonance and fluorescence imaging and for drug delivery, Angew. Chem., Int. Ed. 47 (44) (2008) 8438–8441.
[42] S. Sun, H. Zeng, D.B. Robinson, S. Raoux, G. Li, Monodisperse MFe_2O_4 (M=Fe, Co, Mn) nanoparticles, J. Am. Chem. Soc. 126 (1) (2004) 273–279.
[43] L. Yu, Y. Chen, H. Lin, W. Du, H. Chen, J. Shi, Ultrasmall mesoporous organosilica nanoparticles: morphology modulations and redox-responsive biodegradability for tumor-specific drug delivery, Biomaterials 161 (2018) 292–305.
[44] B. Thangaraj, Z. Jia, L. Dai, D. Liu, W. Du, Effect of silica coating on Fe_3O_4 magnetic nanoparticles for lipase immobilization and their application for biodiesel production, Arab. J. Chem. 12 (8) (2019) 4694–4706.
[45] F. Yang, A. Skripka, M.S. Tabatabaei, S. Hong, F. Ren, Y. Huang, J.K. Oh, S. Martel, X. Liu, F. Vetrone, D. Ma, Magnetic photoluminescent nanoplatform built from large-pore mesoporous silica, Chem. Mater. 31 (9) (2019) 3201–3210.
[46] S.L. Westcott, S.J. Oldenburg, T.R. Lee, N.J. Halas, Formation and adsorption of clusters of gold nanoparticles onto functionalized silica nanoparticle surfaces, Langmuir 14 (19) (1998) 5396–5401.
[47] L. Cui, H. Lin, C. Yang, X. Han, T. Zhang, F. Qu, Synthesis of multifunctional $Fe_3O_4@mSiO_2$@Au core-shell nanocomposites for pH-responsive drug delivery, Eur. J. Inorg. Chem. (36) (2014) 6156–6164, 2014.
[48] I. Roy, P. Kumar, R. Kumar, T.Y. Ohulchanskyy, K.T. Yong, P.N. Prasad, Ormosil nanoparticles as a sustained-release drug delivery vehicle, RSC Adv. 4 (2014) 53498–53504.
[49] R. Zhou, T.Y. Ohulchanskyy, Y. Xu, R. Ziniuk, H. Xu, L. Liu, J. Qu, Tumor-microenvironment-activated NIR-II nanotheranostic platform for precise diagnosis and treatment of colon cancer, ACS Appl. Mater. Interfaces 14 (20) (2022) 23206–23218.
[50] J. Nam, S. Son, L.J. Ochyl, R. Kuai, A. Schwendeman, J.J. Moon, Chemo-photothermal therapy combination elicits anti-tumor immunity against advanced metastatic cancer, Nat. Commun. 9 (2018) 1074.
[51] Y. Deng, Y. Cai, Z. Sun, J. Liu, C. Liu, J. Wei, W. Li, C. Liu, Y. Wang, D. Zhao, Multifunctional mesoporous composite microspheres with well-designed nanostructure: a highly integrated catalyst system, J. Am. Chem. Soc. 132 (24) (2010) 8466–8473.
[52] X. Hou, X. Wang, R. Liu, H. Zhang, X. Liu, Y. Zhang, Facile synthesis of multifunctional $Fe_3O_4@SiO_2$@Au magneto-plasmonic nanoparticles for MR/CT dual imaging and photothermal therapy, RSC Adv. 7 (2017) 18844–18850.
[53] L. Yang, N. Li, K. Wang, X. Hai, J. Liu, F. Dang, A novel peptide/$Fe_3O_4@SiO_2$-Au nanocomposite-based fluorescence biosensor for the highly selective and sensitive detection of prostate-specific antigen, Talanta 179 (2017) 531–537.
[54] F. Lu, L. Yang, Y. Ding, J. Zhu, Highly emissive Nd^{3+}-sensitized multilayered upconversion nanoparticles for efficient 795 nm operated photodynamic therapy, Adv. Funct. Mater. 26 (26) (2016) 4778–4785.
[55] F. Lu, L. Li, M. Zhang, C. Yu, Y. Pan, F. Cheng, W. Hu, X. Lu, Q. Wang, Q. Fan, Confined semiconducting polymers with boosted NIR light-triggered H_2O_2 production for hypoxia-tolerant persistent photodynamic therapy, Chem. Sci. 15 (2024) 12086–12097.
[56] Y. Xu, K. Wang, Y. Zhu, J. Wang, D. Ci, M. Sang, Q. Fang, H. Deng, X. Gong, K.C. F. Leung, S. Xuan, Size-dependent magnetomechanically enhanced photothermal antibacterial effect of Fe_3O_4@Au/PDA nanodurian, Dalton Trans. 52 (2023) 17148–17162.
[57] F. Faiz, J. Qiao, H. Lian, L. Mao, X. Cui, A combination approach using two functionalized magnetic nanoparticles for speciation analysis of inorganic arsenic, Talanta 237 (2022) 122939.
[58] Q. Cheng, L. Yue, J. Li, C. Gao, R. Wang, Supramolecular tropism driven aggregation of nanoparticles in situ for tumor-specific bioimaging and photothermal therapy, Small 17 (43) (2021) 2101332.
[59] Y. Sahoo, A. Goodarzi, M.T. Swihart, T.Y. Ohulchanskyy, N. Kaur, E.P. Furlani, P. N. Prasad, Aqueous ferrofluid of magnetite nanoparticles: fluorescence labeling and magnetophoretic control, J. Phys. Chem. B 109 (9) (2005) 3879–3885.
[60] R. Kumar, I. Roy, T.Y. Ohulchanskyy, L.N. Goswami, P.N. Prasad, Covalently dye-linked, surface-controlled, and bioconjugated organically modified silica nanoparticles as targeted probes for optical imaging, ACS Nano 2 (3) (2008) 449–456.
[61] Q. Zheng, T.Y. Ohulchanskyy, Y. Sahoo, P.N. Prasad, Water-dispersible polymeric structure co-encapsulating a novel hexa-peri-hexabenzocoronene core containing chromophore with enhanced two-photon absorption and magnetic nanoparticles for magnetically guided two-photon cellular imaging, J. Phys. Chem. C 111 (45) (2007) 16846–16851.
[62] A. Grebinyk, S. Prylutska, S. Grebinyk, Y. Prylutskyy, M. Frohme, Complexation with C60 fullerene increases doxorubicin efficiency against leukemic cells in vitro, Nanoscale Res. Lett. 14 (2019) 91.
[63] A.I. Baba, C. Cătoi, Comparative Oncology, Bucharest (RO), The publishing house of the Romanian academy, 2007, pp. 1–32.
[64] D. Liao, Y. Luo, D. Markowitz, R. Xiang, R.A. Reisfeld, Cancer associated fibroblasts promote tumor growth and metastasis by modulating the tumor immune microenvironment in a 4T1 murine breast cancer model, PLoS One 4 (2009) e7965.
[65] R.A. Glabman, P.L. Choyke, N. Sato, Cancer-associated fibroblasts: tumorigenicity and targeting for cancer therapy, Cancers 14 (16) (2022) 3906.
[66] B. Zhou, S. Yan, S. Zheng, Intrathoracic extramedullary hematopoiesis mimicking intrathoracic tumors: a case report, Oncol. Lett. 7 (6) (2014) 1984–1986.
[67] W.C. Cho, S. Mandavilli, Intratumoral extramedullary hematopoiesis in solitary fibrous tumor of the breast, Breast J. 26 (2019) 755–758.
[68] Z. Chen, X. Cheng, L. Yang, X. Cheng, B. Zhu, H. Long, Mechanism and effects of extramedullary hematopoiesis on anti-tumor immunity, Cancer Biol. Med. 20 (7) (2023) 477–482.